Supporting Information

Phosphor-Nitrogen Dual-Doping Engineering in Hard Carbon Microspheres for Enhanced Sodium-Ion Storage

Yuanqi Ding[a b], Yanan Cui[a c], Zhonglei Du[a c], Quanxiu Liu[a c], Yuan Li[a b], Pengbo Liu[a b], Menghan Zhan[b], Dehong Chen[b], Yaodi Zhu[b], Lingbo Zong[a c] *, Pavel Novikov[d], Sardor Donaev[e], Munavvar Iskandarova[e], Nuritdin Amirkulov[e], Lei Wang[a c] *, Bin Li[a b] *

[a]*International Science and Technology Cooperation Base of Eco-chemical Engineering and Green Manufacturing, Qingdao University of Science and Technology, Qingdao 266042, China*

[b]*College of Materials Science and Engineering, Qingdao University of Science and Technology, Qingdao 266042, China*

[c]*College of Chemistry and Molecular Engineering, Qingdao University of Science and Technology, Qingdao 266042, China*

[d]*Scientific and Educational Center "Mechanical Engineering Technologies and Materials", Petersburg Polytechnic University, St. Petersburg, 195251, Russia*

[e]*Tashkent State Technical University, Tashkent 100095, Tashkent, Uzbekistan*

E-mail: lingbozong@qust.edu.cn; inorchemwl@126.com; binli@qust.edu.cn

Experimental

Materials and methods. Synthesis of PNHC/PHC/NHC/HC: A mixed solution (100 mL) with a defined ethanol-water ratio was heated to 60 °C. Ethanol–water ratios of 0:5, 1:4, 2:3, 3:2, 4:1 and 5:0 was used during the synthesis of the precursor. A gel was obtained by stirring sodium carboxymethyl cellulose (CMC) with 200 mg of L-lysine, after which 5 mL of phytic acid (70%), 3 g of resorcinol and 4.2 mL of formaldehyde (37 wt%) were successively introduced. The resulting mixture underwent continuous stirred at 60 °C for 4 h, followed by centrifugation and vacuum drying at the same temperature for 12 h and was subsequently heated at 1100 °C for 2 h under an argon atmosphere with 5 °C min^{-1}. After natural cooling, P/N co-doped hard carbon (PNHC) was obtained. For comparison, samples prepared without L-lysine were designated as PHC, while those prepared with L-lysine only were designated as NHC. And an undoped hard carbon (HC) was prepared under identical conditions but without adding L-lysine or phytic acid. For the samples synthesized with ethanol–water ratios of 4:1 and 5:0, the products became extremely rigid after post-treatment and remained too hard to grind even after carbonization. As these samples could not be processed for further characterization, they were not included in the discussion.

Materials characterizations: The surface and structural features of the samples were characterized by combined scanning and transmission electron microscopy (SEM, Regulus 8100; TEM, JEM-F200), with HRTEM employed for detailed lattice analysis and EDX mapping used to determine elemental distribution. X-ray diffraction (XRD, D/MAX/2500PC, Cu Kα radiation, 10–80°, 5° min^{-1}) was performed to determine the crystalline phases. Raman spectroscopy (inVia Qontor) was employed to characterize the graphitization degree and defect density. The surface chemical states were analyzed using X-ray photoelectron spectroscopy (XPS, Kratos AXIS SUPRA, UK) and the binding energies were calibrated with reference to the C 1s peak at 284.8 eV. The specific surface area and pore size distribution were analyzed using Brunauer–Emmett–Teller (BET) measurements (Micromeritics ASAP 2020) based on N_2 adsorption–desorption isotherms.

Electrochemical measurements: The anode was prepared by mixing Super P, polyvinylidene fluoride (PVDF) and hard carbon binder in a mass ratio of 1:1:8. After the addition of N-methyl-2-pyrrolidone (NMP), the resulting paste was then coated onto Cu foil, with subsequent drying under vacuum at 80 °C for 12 h. The mass loading of the electrode was controlled within 1.3-1.6 mg cm^{-2}. Under an argon-protected atmosphere (H_2O < 0.1 ppm, O_2 < 0.1 ppm), CR2032 coin cells were prepared using 1 M $NaPF_6$ in diglyme as the electrolyte, with GF/A and metallic sodium serving as the

separator and counter electrode, respectively. For the assembly of full cells, commercial $Na_3V_2(PO_4)_3$ (NVP) served as the cathode, while PNHC functioned as the anode. The anode electrode had a diameter of 12 mm, while the cathode electrode had a diameter of 10 mm. The PNHC electrode was pre-cycled five times at a current density of 0.05 A g^{-1} to reduce irreversible sodium loss. The mass loading of the cathode active material was 3.65-3.48 mg cm^{-2}. The N/P ratio was controlled within 1.05-1.1 to maintain charge balance. The full-cell utilized identical electrolyte and separator compositions to ensure consistency with the half-cell. All electrochemical measurements were conducted over a voltage range of 0.01-3.0 V (vs. Na^+/Na) for half-cells and 2.0-4.0 V for full cells. A CHI660D electrochemical workstation was employed to record cyclic voltammetry (CV) curves at scan rates from 0.1 to 1.5 mV s^{-1}. Galvanostatic charge–discharge (GCD) measurements were carried out using a LAND CT2001A (Wuhan, China). Electrochemical impedance spectroscopy (EIS) was a conducted on the Ec-lab (BioLogic) within a 100 kHz-0.01 Hz frequency window at 5 mV amplitude The tests were performed at room temperature.

DFT: The spin-polarized DFT computations were executed within the framework of the Vienna *Ab initio* Simulation Package (VASP), adopting the PAW formalism and a cutoff energy of 450 eV for plane-wave expansion. The exchange–correlation interactions were described within the generalized gradient approximation (GGA) employing the Perdew–Burke–Ernzerhof (PBE) functional. Brillouin zone integration employed k-point grids generated by VASPKIT, ensuring a spacing below 0.04 $Å^{-1}$. Geometry optimization continued until the energy and force converged to 10^{-5} eV and 0.02 eV $Å^{-1}$. Na^+ migration energy barriers were assessed via the climbing-image nudged elastic band (CI-NEB) method, employing three interpolated images for the NHC, PHC and PNHC models. All structures were visualized with VESTA.

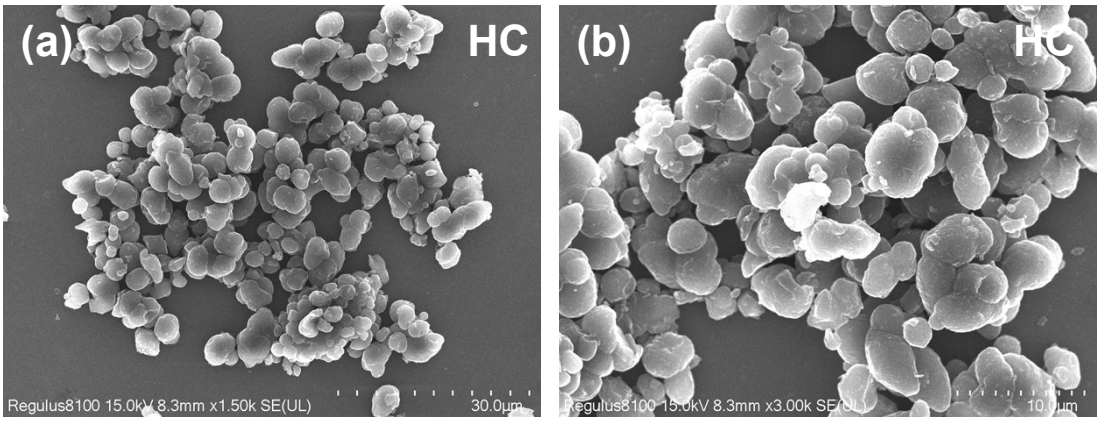

Fig. S1. SEM of HC

Compared with Fig. 2a–c, the resin obtained without any dopants shows an irregular morphology, whereas the introduction of N and P gradually leads to more uniform particle formation with reduced particle size.

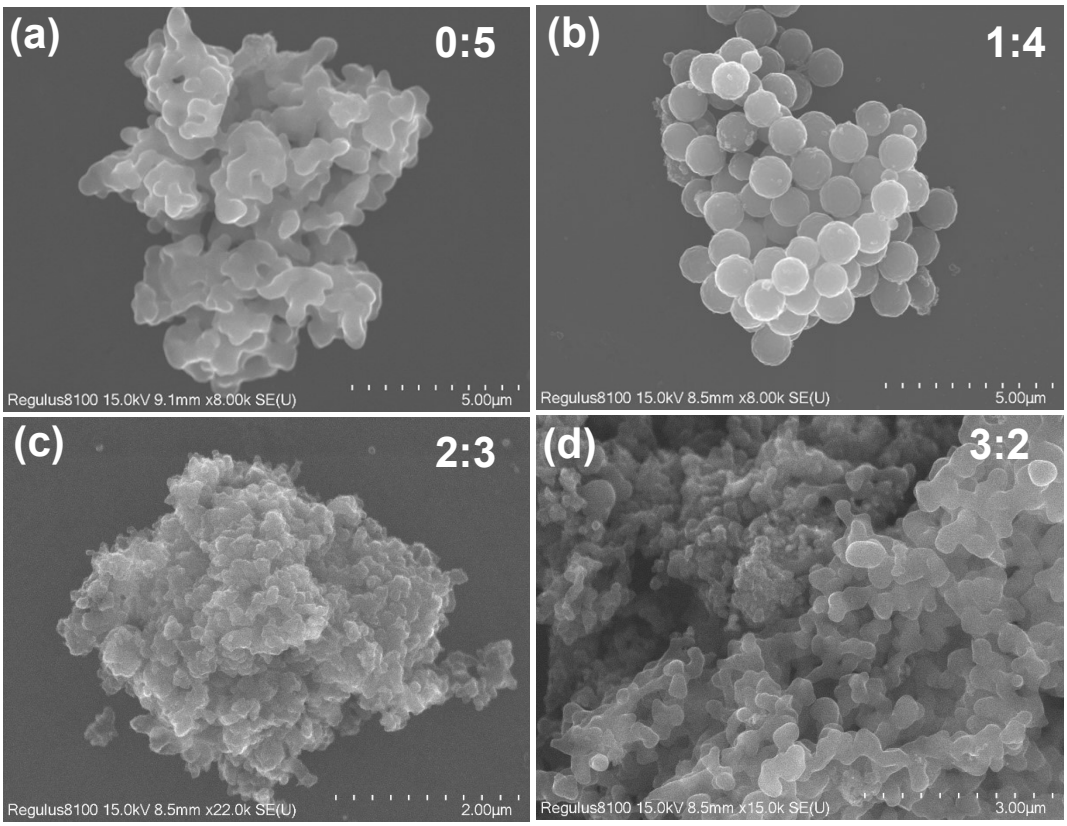

Fig. S2. SEM (a) pure water. (b) V ethanol: V water ratio of 1:4. (c) V ethanol: V water ratio of 2:3. (d) V ethanol: V water ratio of 3:2.

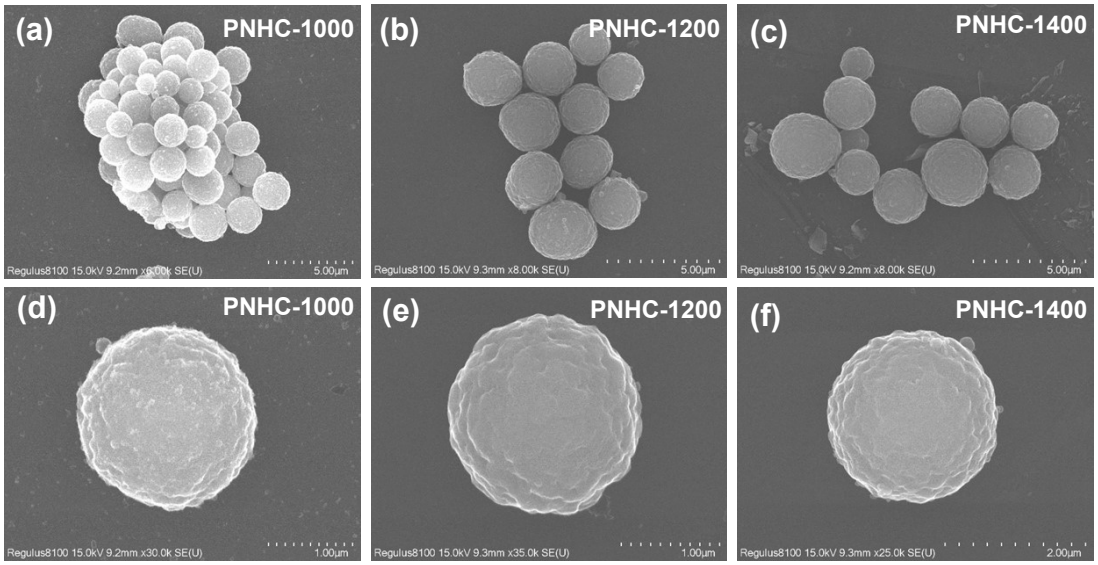

Fig. S3. SEM image of (a,d) PNHC-1000. (b,e) PNHC-1200. (c,f) PNHC-1400.

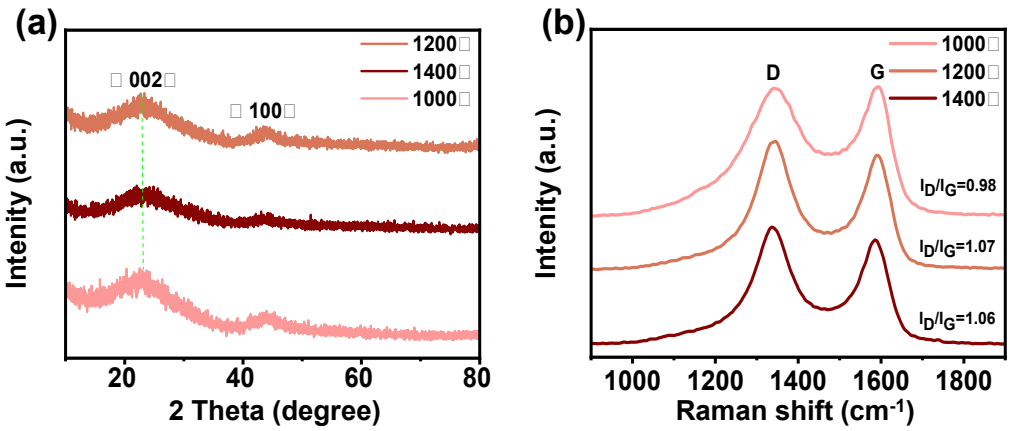

Fig. S4. Structural characterizations of PNHC-1000. NHC-1200 and PNHC-1400. (a) XRD patterns. (b) Raman spectra.

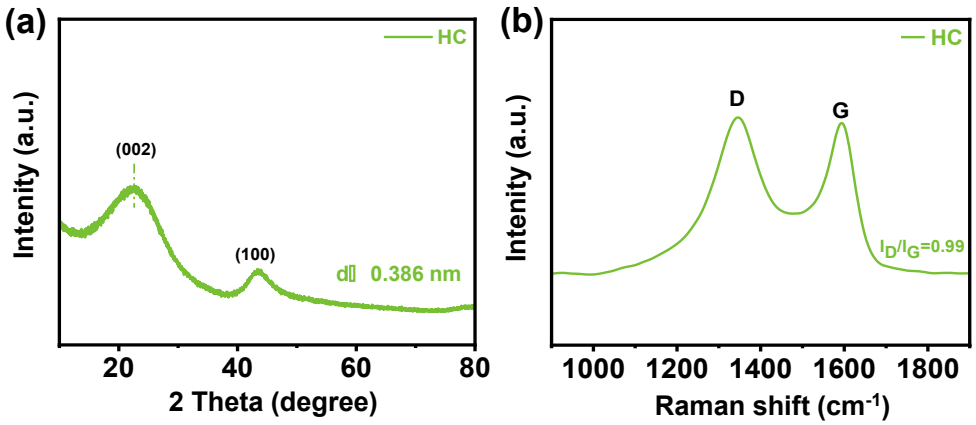

Fig. S5. Structural characterizations of HC (a) XRD patterns. (b) Raman spectra.

XRD analysis indicates that the interlayer spacing of HC and NHC without phosphorus doping is quite similar. With the introduction of phosphorus, the interlayer distance is increased, suggesting that P incorporation expands the carbon layers, which can facilitate Na^+ intercalation. Raman spectroscopy shows that pristine HC exhibits a lower defect degree compared to NHC, PHC, and PNHC, indicating that the introduction of nitrogen and phosphorus increases the disorder and defect density on the carbon surface.

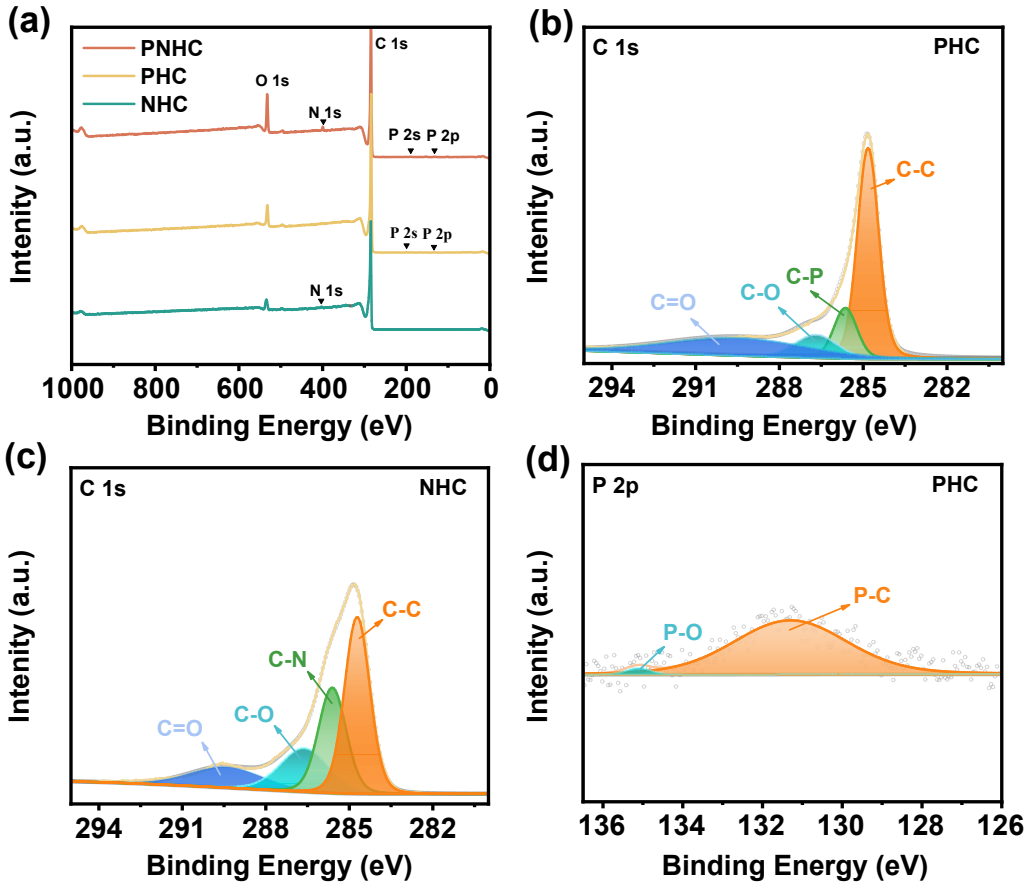

Fig. S6. (a) XPS survey spectra. (b, c) C 1s of PHC and NHC. (d) P 2p of PHC.

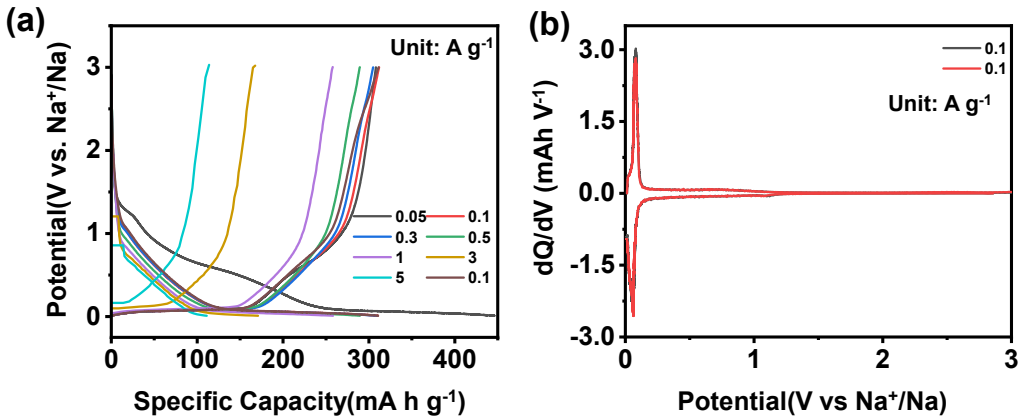

Fig. S7. (a) GCD curves at different current densities and (b)the corresponding *d*Q/*d*V profiles of PNHC.

After the rate test from 0.05 to 5 A g^{-1}, the GCD profile recorded again at 0.1 A g^{-1}(brown curve) almost completely overlaps with the initial 0.1 A g^{-1} curve (red curve). The corresponding *d*Q/*d*V curves also coincide well with each other, demonstrating that the sodium-storage mechanism and characteristic voltage features remain essentially unchanged during high-rate cycling. These observations indicate that PNHC preserves stable reaction pathways even under large current densities, and its outstanding rate capability is not dictated by specific surface area alone. Instead, the combined effects of P/N co-doping—such as the enlarged interlayer spacing and increased N-6 active sites—effectively mitigate the kinetic limitations typically associated with lower SSA in hard carbon.

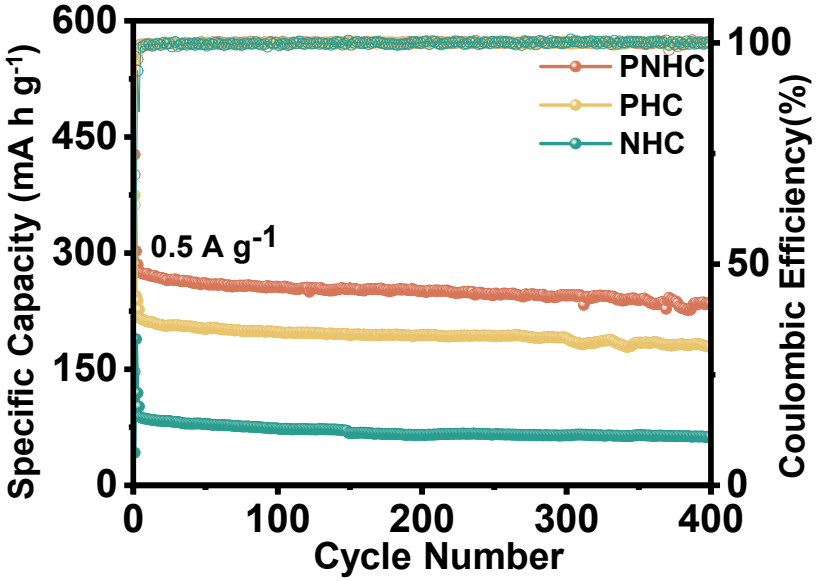

=

Fig. S8. Cyclic performances at 0.5A g^{-1}.

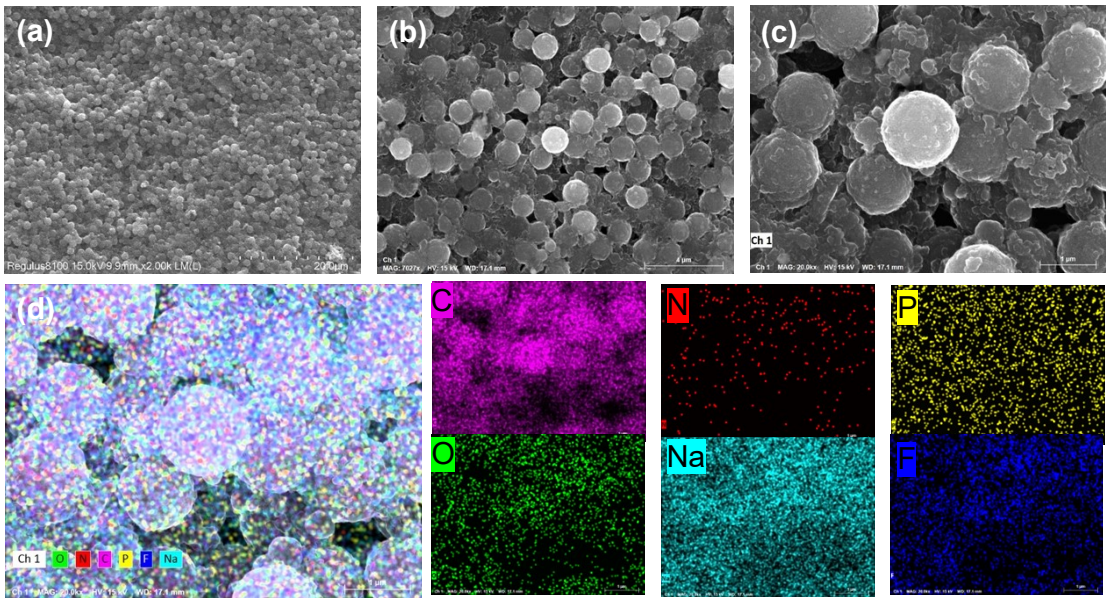

Fig. S9. (a-c) SEM images of PNHC electrode after 5000 cycles at 5.0 A g^{-1}. (d) EDS elemental maps of C, N, P, O, Na, and F for NPUCS electrode after 5000 cycles at 5.0 A g^{-1}.

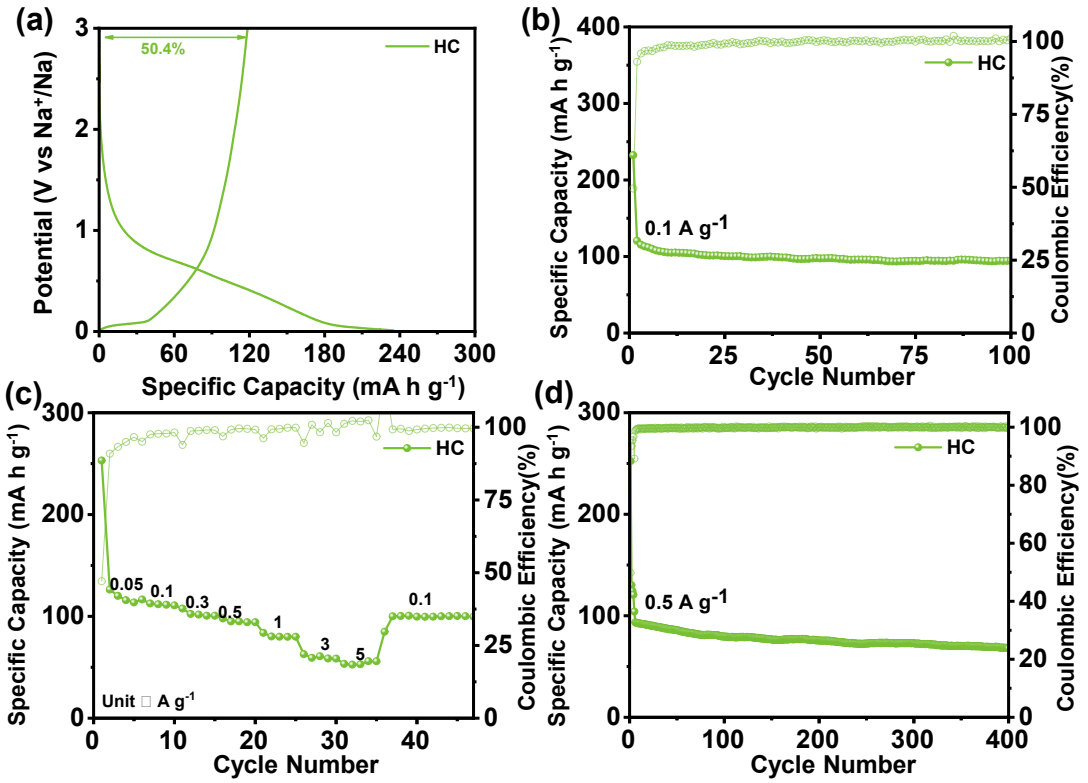

Fig. S10. Electrochemical evaluation of the HC electrodes as SIB anodes in half cells. (a) The GCD curves at 0.05 A g^{-1}. (b) Cyclic performances at 0.1A g^{-1}. (f) Rate performances. (g) Cyclic performances at 0.5A g^{-1}.

The undoped HC exhibits a low ICE of only 50.4%, which is lower than that of NHC, PHC and PNHC. GCD analysis shows that the capacity contribution from the low-voltage plateau region is much smaller than that of PHC and PNHC, indicating that P incorporation increases the interlayer spacing and enhances capacity below 0.1 V. Meanwhile, N doping contributes to the sloping region above 0.1 V, resulting in the highest overall capacity observed for PNHC. After 100 cycles at 0.1 A g^{-1}, the reversible capacity of HC is only 95.4 mAh g^{-1}, with a capacity retention of 82.7%, which is lower than those of the doped samples. Rate capability tests also reveal that HC underperforms compared to the other materials. At a higher current density of 0.5 A g^{-1} over 400 cycles, HC retains a capacity of 67.7 mAh g^{-1}, which is still lower than PHC and PNHC, demonstrating that the expanded interlayer spacing induced by P doping facilitates Na^+ intercalation at high current densities. Collectively, comparison of ICE,

cycling stability, and rate performance confirms that the synergistic effect of N and P doping endows PNHC with superior electrochemical performance.

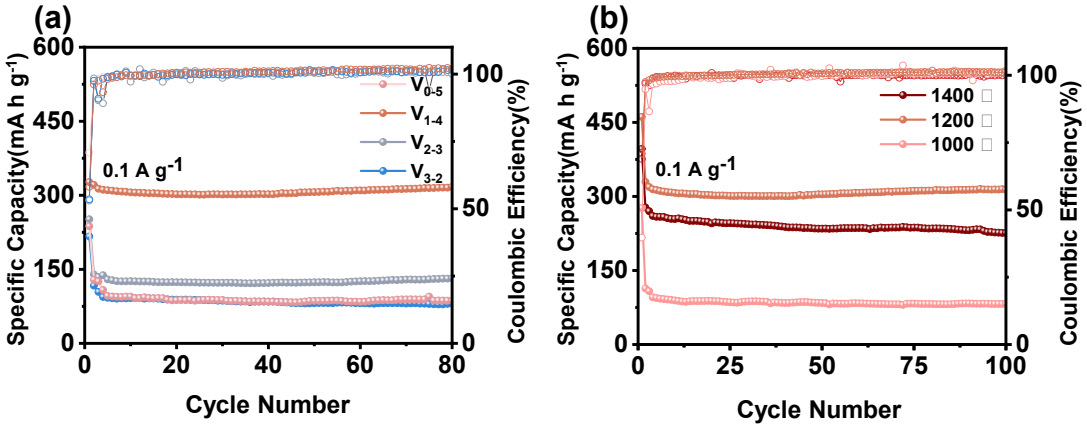

Fig. S11. Cyclic performance at 0.1 A g^{-1} of (a)samples with different ethanol-water ratios and (b)samples prepared at different temperatures.

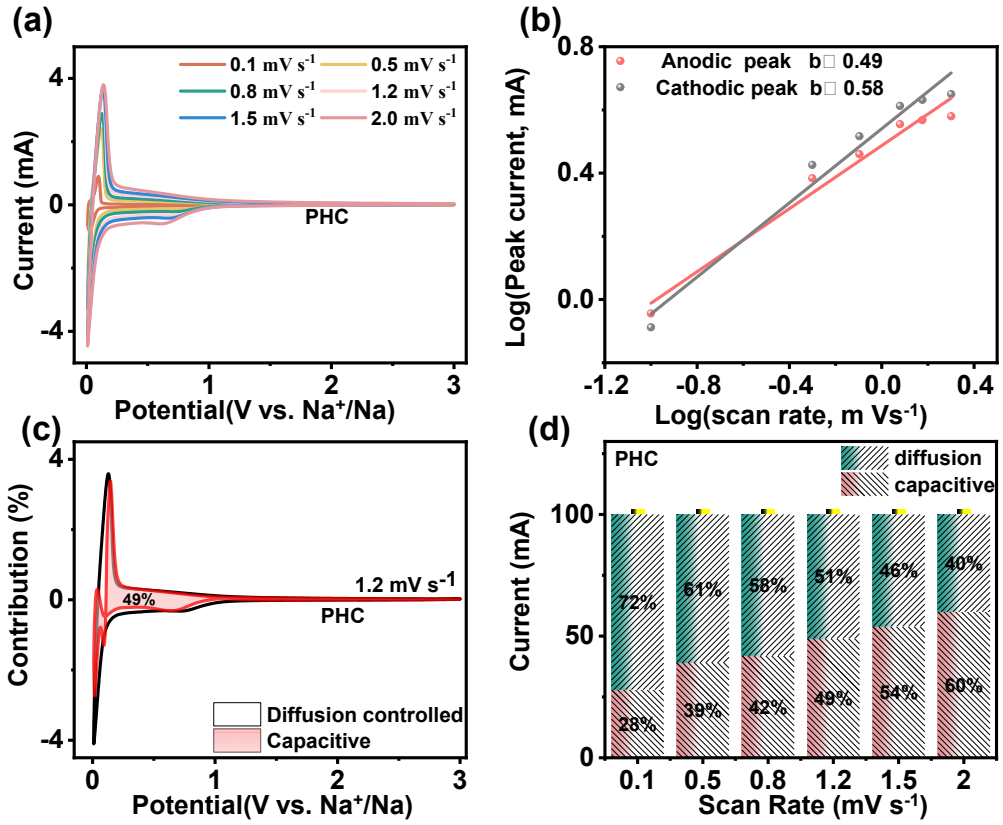

Fig. S12. The CV curves at different scanning rates: (a) PHC. Plots of log (sweep rate) versus log (current): (b) PHC. (c) pseudocapacitive and diffusive contribution at 1.2 mV s^{-1} of PNHC. Contribution of diffusion- and capacitive-controlled capacity of (d) PHC electrode at different scan rates.

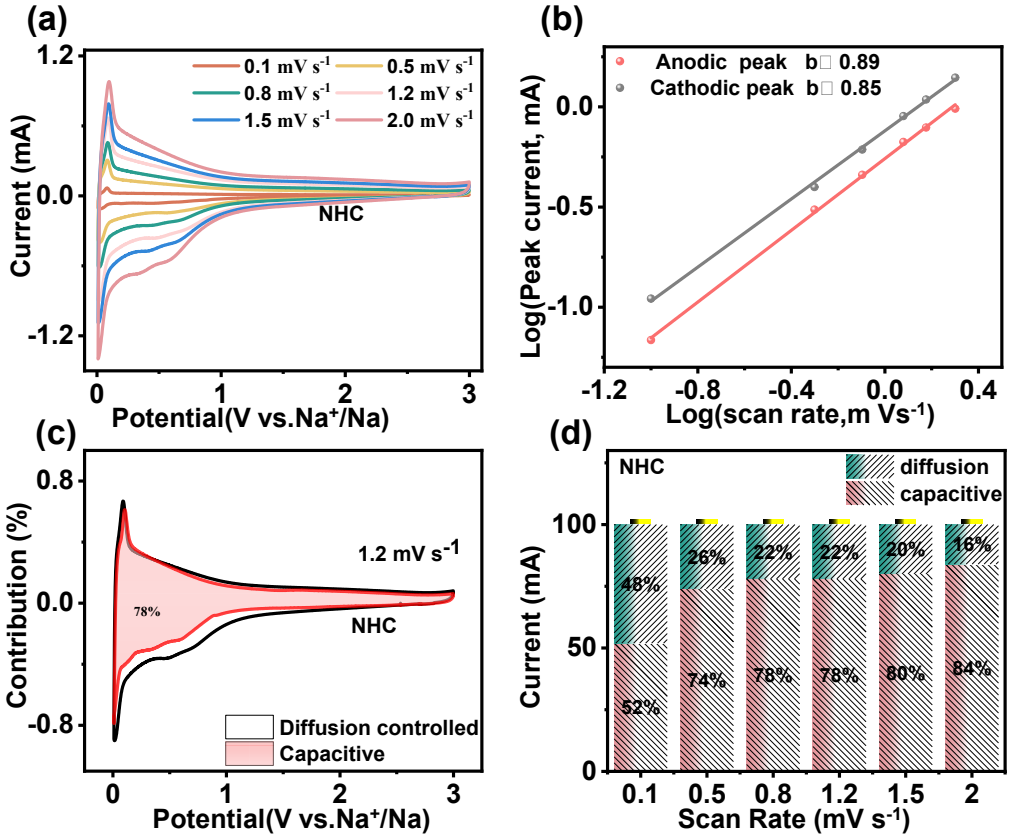

Fig. S13. The CV curves at different scanning rates: (a) NHC. Plots of log (sweep rate) versus log (current): (b) NHC. (c) pseudocapacitive and diffusive contribution at 1.2 mV s^{-1} of PNHC. Contribution of diffusion- and capacitive-controlled capacity of (d) NHC electrode at different scan rates.

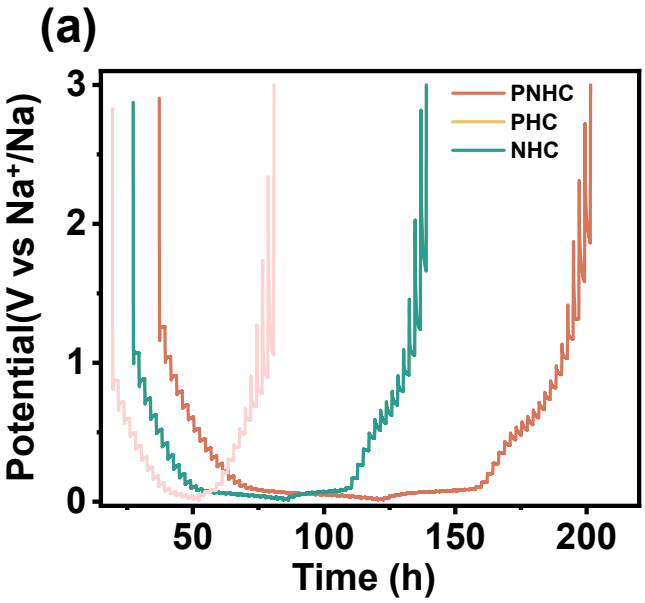

Fig. S14. GITT of the sample

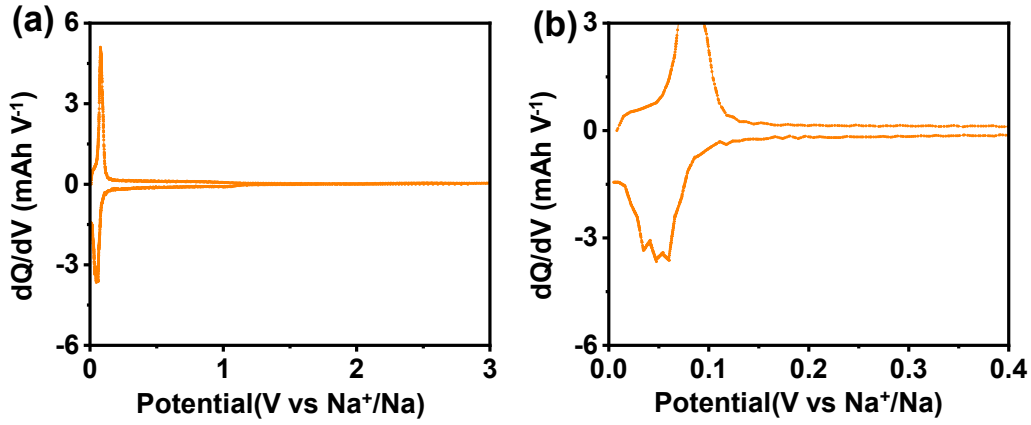

Fig. S15. (a) *d*Q/*d*V profile of the PNHC electrode; (b) enlarged view of the 0.1-0.01 V region.

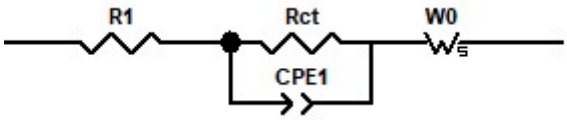

Fig. S16. Equivalent circuits

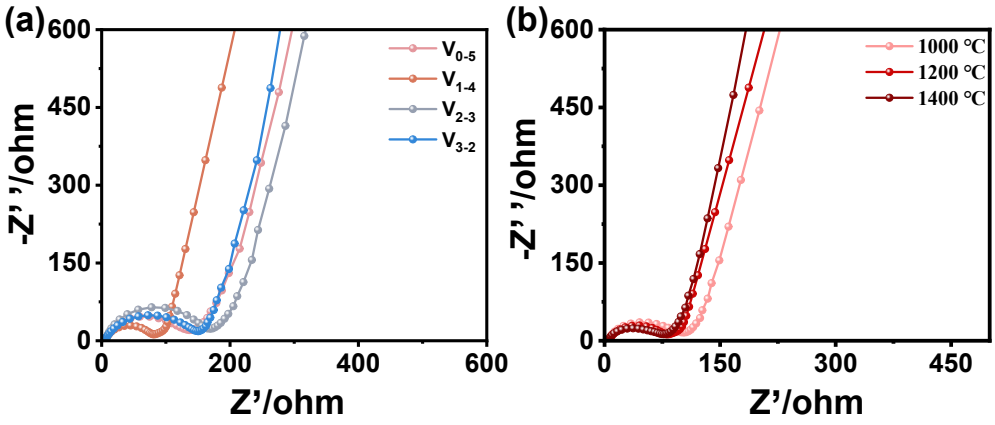

Fig. S17. Nyquist plots of samples prepared under different ethanol–water ratios and carbonization temperatures.

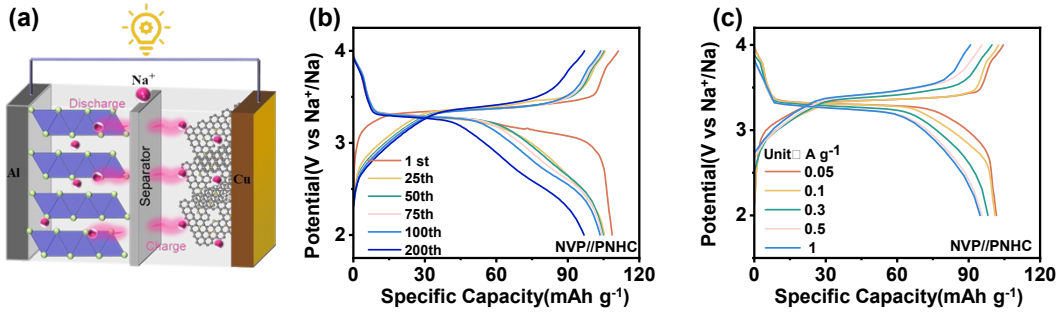

Fig. S18. (a) full cell model. (b)GCD curves of NVP//PNHC at different cycle numbers and (c) various current densities.

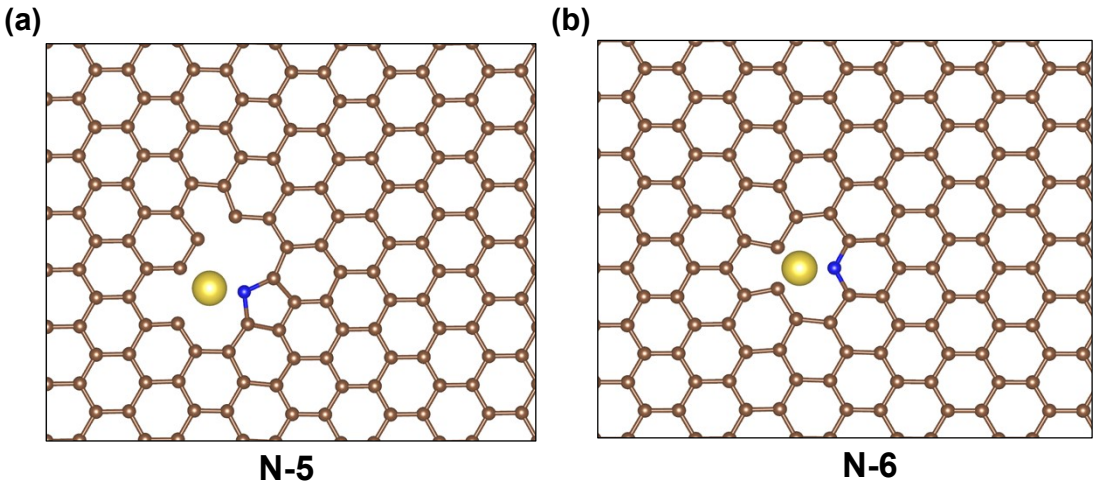

Fig. S19. DFT calculations: structures of Na+ adsorbed on (a) N-5, (b) N-6.

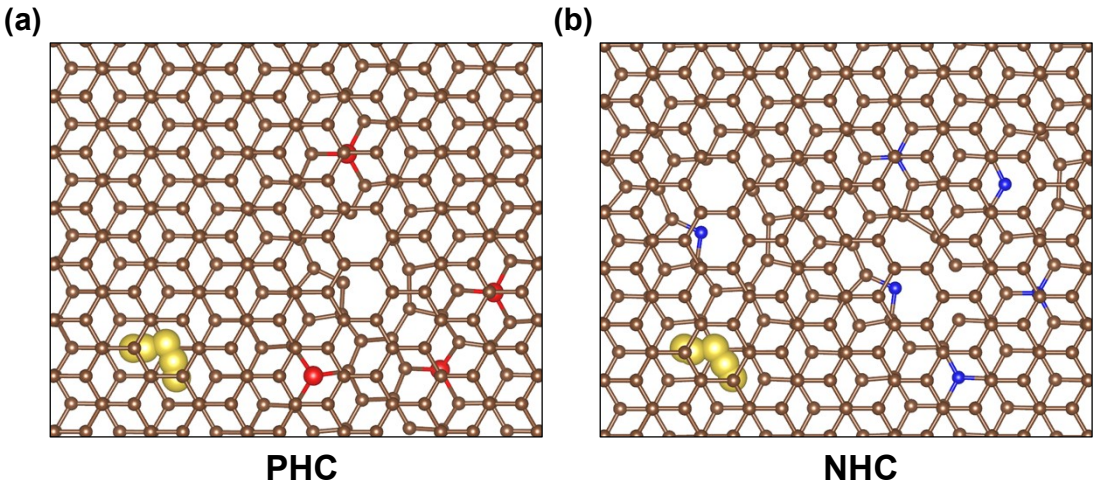

Fig. S20. Top view of Na-ion diffusion path in (a) PHC defect-carbon sheet and (b) NHC defect-carbon sheet

Table S1. Calculated Rct values obtained by fitting the Nyquist plots.

Materials	**Rct（Ω）**
$V_{0\text{-}5}$	110
$V_{1\text{-}4}$	67.87
$V_{2\text{-}3}$	141
$V_{3\text{-}2}$	147
1000℃	80.26
1200℃	67.87
1400℃	58.76

Table S2. Comparison of the electrochemical performance of NVP//PNHC full cells with previously reported hard carbon anodes for sodium-ion batteries.

Materials	Energy density ($Wh\ kg^{-1}$)	Per-cycle retention (%)	Reference
NVP//NC@MESP	159.4	73.5	Ref [1]
NVP//HC-3	191.2	99.51	Ref [2]
NVP//HCUP-40	223.6	87.5	Ref [3]
NVP//PCHC-10	201.3	95.4	Ref [4]
NVP//ZHCS6-13	205.8	75	Ref [5]
NVP//ZGHC1500	260.4	88.7	Ref [6]
NFM//R-NH-1400	166.8	95.2	Ref [7]
NVP//HOBAHC-30%	217.2	90.9	Ref [8]
NVP//PNHC	221.2	86.8	This work

References:

1 Z. C. Hu, Y. F. Yuan, K. Q. Du, G. S. Cai, B. X. Wang, M. Zhu and Y. B. Chen, *Journal of Energy Storage*, 2026, **141**, 119440.

2 H. Pei, R. Wang, Y. Li, Y. Xue, Y. Chen, J. Jiang, X. Kong, Q. Zhuang and Z. Ju, *Journal of Colloid and Interface Science*, 2025, **690**, 137359.

3 Y. Liu, S. Dai, J. Deng, D. Jiang, X. Ji, Q. Meng, H. Wang and L. Liu, *Journal of Colloid and Interface Science*, 2025, **686**, 136–150.

4 D. Sun, L. Zhao, Y. Yang, C. Lu, C. Xu, Z. Xiao and X. Ma, *Materials Reports: Energy*, 2025, **5**, 100330.

5 Z. Zhang, Y. Wang, K. Tang, Z. Chen, X. Li, N. Zhang, Z. Wu and X. Xie, *Nanoscale Horiz.*, 2025, **10**, 824–834.

6 J. Cui, W. Li, P. Su, X. Song, W. Ye, Y. Zhang and Z. Chen, *Advanced Energy Materials*, 2025, **15**, 2502082.

7 X. Lei, L. Zhang, X. Guo, Q. Tian, Y. Yang, Y. Yi, J. Shi, J. Zhong, X. Cao, F. Wu, X. Wang and S. Wang, *Sustainable Materials and Technologies*, 2025, e01779.

8 X. Chen, C. Bao, K. Shi, J. Xiao, C. Wen, D. Huang, C. Zhang, F. Wang, H. Quan, Q. Liu, H. Liu, J. Liu and C. Ye, *Chemical Engineering Journal*, 2025, **523**, 168400.